Available online at www.sciencedirect.com
SCIENCE DIRECT®
Icarus 181 (2006) 145–155
ICARUS
www.elsevier.com/locate/icarus

Radar and optical observations and physical modeling of near-Earth Asteroid 10115 (1992 SK)

Michael W. Busch [a,*], Steven J. Ostro [b], Lance A.M. Benner [b], Jon D. Giorgini [b], Raymond F. Jurgens [b], Randy Rose [b], Christopher Magri [c], Petr Pravec [d], Daniel J. Scheeres [e], Stephen B. Broschart [e]

[a] *Division of Geology and Planetary Science, California Institute of Technology, Mail Code 150-21, Pasadena, CA 91125, USA*
[b] *Jet Propulsion Laboratory, California Institute of Technology, Pasadena, CA 91109-8099, USA*
[c] *University of Maine at Farmington, Preble Hall, 173 High St., Farmington, ME 04938, USA*
[d] *Astronomical Institute, Academy of Sciences of the Czech Republic, Fricova 1, CZ-25165 Ondřejov, Czech Republic*
[e] *Department of Aerospace Engineering, University of Michigan, 1320 Beal Avenue, Ann Arbor, MI 48109, USA*

Received 28 August 2005; revised 20 October 2005

Available online 19 December 2005

Abstract

We estimate Asteroid 1992 SK's physical properties from delay–Doppler images and Doppler-only echo spectra obtained during March 22–27, 1999, at Goldstone and from optical lightcurves obtained during February–March 1999 at Ondřejov Observatory. The images span only about 15° of sky motion and are not strong, but they place up to twenty 40 m by 160 m pixels on the asteroid and have complete rotational phase coverage. Our analysis establishes that the radar observations are confined to subradar latitudes between −20° and −40°. The echo spectra and optical lightcurves span ∼80° of sky motion, which provides important geometric leverage on the pole direction. The lightcurves are essential for accurate estimation of the asteroid's shape and spin state. We estimate the asteroid's period to be 7.3182 ± 0.0003 h and its pole direction to be at ecliptic longitude, latitude = $(99° \pm 5°, -3° \pm 5°)$. The asteroid is about 1.4 km in maximum extent and mildly asymmetric, with an elongation of about 1.5 and relatively subdued topography. The OC radar albedo is 0.11 ± 0.02 and the SC/OC ratio is 0.34 ± 0.05. The current orbital solution permits accurate identification of planetary close approaches during 826–2690. We use our model to predict salient characteristics of radar images and optical lightcurves obtainable during the asteroid's March 2006 approach.
© 2005 Elsevier Inc. All rights reserved.

Keywords: Asteroids; Radar; Asteroids, rotation; Surfaces, asteroids

1. Introduction

1992 SK, an S-class near-Earth asteroid (NEA) (Binzel et al., 2004), was discovered by E. Helin and J. Alu at Palomar in September 1992 (Helin, 1992). Subsequent optical observations and investigation of archival plates, including a precovery from 1952, refined the orbit and indicated that 1992 SK would make an approach to within 0.06 AU in 1999. Observations were planned at both Goldstone and Arecibo, but mechanical failure prevented the Arecibo observations. Goldstone observations during March 22–27 using the 70-m antenna and 8560-MHz transmitter provided both Doppler-only (continuous wave or CW) echo spectra and delay–Doppler images of the object.

Ondřejov Observatory in the Czech Republic obtained R-band optical lightcurves as part of their NEA photometry program (described in Pravec et al., 1998) on February 8–10, 15 and March 11 and 13, 1999 (Table 1). The lightcurves indicate a synodic period of 7.318 ± 0.002 h and suggest an elongated, mildly asymmetric shape. The lightcurves were obtained at solar phase angles between 40° and 70°, so their sensitivity to morphology and topographic structure complements that of the radar observations.

* Corresponding author.
E-mail address: busch@caltech.edu (M.W. Busch).

0019-1035/$ – see front matter © 2005 Elsevier Inc. All rights reserved.
doi:10.1016/j.icarus.2005.10.024

Table 1
Optical observations

Date	Time interval (UTC)	Phase angle	RA	DEC	Delta (AU)	r (AU)
1999 Feb 7–8	23:30–01:30	41°	188°	53°	0.305	1.195
1999 Feb 8–9	21:50–06:00	42°	189°	54°	0.298	1.190
1999 Feb 9	20:30–22:00	42°	189°	54°	0.292	1.184
1999 Feb 15–16	18:00–03:00	44°	190°	57°	0.252	1.153
1999 Mar 11–12	20:00–00:30	69°	177°	78°	0.108	1.027
1999 Mar 12–13	22:00–04:00	71°	173°	80°	0.098	1.022

Note. Observing intervals, solar phase angles, sky positions, Earth-object, and object–Sun distances for the optical observations.

Table 2
Radar observations

Type	Resolution	Orbital solution	Time (UTC)	Runs	Subradar latitude	Rotation phase coverage
CW	0.98 Hz	10	Mar 22 18:38–Mar 22 19:26	12	−29°	196°–258°
Ranging	10 µs	10	Mar 22 19:50–Mar 22 20:27	17	−29°	
Ranging	11 µs	10	Mar 22 20:40–Mar 22 21:02	10	−29°	
CW	0.49 Hz	12	Mar 23 17:07–Mar 23 17:19	6	−28°	250°–258°
Ranging	10 µs	12	Mar 23 17:51–Mar 23 18:00	5	−28°	
CW	0.49 Hz	12	Mar 23 18:29–Mar 24 04:36	172	−28°	∼1.5 rotations
CW	0.49 Hz	12	Mar 24 17:51–Mar 24 18:10	10	−28°	23°–40°
Ranging	10 µs	12	Mar 24 19:12–Mar 24 19:19	4	−28°	
Ranging	1 µs	12	Mar 24 19:42–Mar 25 19:57	8	−28°	
Ranging	0.5 µs	12	Mar 24 20:16–Mar 25 20:29	7	−28°	
CW	0.49 Hz	12	Mar 24 21:31–Mar 25 00:21	59	−28°	203°–351°
CW	0.49 Hz	12	Mar 25 16:15–Mar 25 16:33	12	−27°	350°–365°
Delay–Doppler	0.25 µs × 5.0 Hz	12	Mar 25 17:05–Mar 25 18:29	43	−27°	42°–92°
Delay–Doppler	0.25 µs × 2.0 Hz	12	Mar 25 18:47–Mar 26 03:31	154	−27°	∼1.25 rotations
CW	0.49 Hz	12	Mar 26 18:22–Mar 26 18:40	14	−27°	92°–107°
Delay–Doppler	0.25 µs × 2.0 Hz	12	Mar 26 18:55–Mar 26 23:36	123	−27°	∼2 rotations

Note. Rotation phase is referenced to the $+x$ axis of our model.

The lightcurve-derived period of about 7.32 h and our long Goldstone tracks (Table 2) resulted in a radar data set with complete rotation phase coverage. On two of the days, individual tracks covered more than a full rotation. During the first three tracks, we obtained only CW data (Fig. 1), in both same-sense as transmitted circular (SC) and opposite-sense (OC) polarizations. The circular polarization ratio SC/OC was 0.34 ± 0.05, about average for an S-class NEA (Ostro et al., 2002), indicating surface roughness comparable to Eros' (Magri et al., 2001). We used only the OC data for our shape modeling (Fig. 2), since the SC data are roughly three times weaker and therefore do not provide much additional information.

We used our CW data, which we believe to be better calibrated than our imaging data, for our radar cross-section estimates. The cross-section varies with rotation phase, suggesting asymmetry in the object's shape, and averages 0.38 km^2. We can use this value, after modeling the shape, to derive an estimate of the asteroid's radar albedo. The CW data were also used to refine the ephemeris prior to further observations.

On March 25 and 26, we shifted to OC delay–Doppler imaging. We formed delay–Doppler images that are sums of 7 to 10 transmit–receive cycles and cover a total of 15 to 20 min. The images are smeared over about 10° of rotational phase, but place a maximum of 10 range pixels on the target, so rotational smearing is not significant. Fig. 3 shows a collage of the delay–Doppler images used in our analysis.

2. Astrometry and refined orbit

Table 3 presents radar astrometry obtained from the physical modeling described below. Briefly, the delay–Doppler locations of the asteroid's center of mass in each data frame were treated as free parameters and we used the change in chi-square as a function of those parameters to set our 1-σ errors.

Table 4 shows orbital elements estimated from the available radar and optical astrometry. With six days of radar observations and a fifty-year optical observation arc, close approaches can be predicted accurately from 826 until almost 2700. With the long baseline of optical astrometry, radar astrometry does not lengthen the interval very much. The 1999 approach was the closest until 2059, although one within 0.11 AU will take place on March 15, 2006, providing an observing opportunity described at the end of this paper.

3. Modeling approach

We modeled the radar and photometric data using shape reconstruction software originally developed by Hudson (1993) and refined during the last two years by C. Magri. This SHAPE software uses nonlinear weighted least-squares to fit a model to CW echo spectra, delay–Doppler images, and lightcurves. Radar images cannot be directly transformed into a shape model, due to the geometrical nature of the delay–Doppler projection (Ostro et al., 2002). Instead, models are used to produce

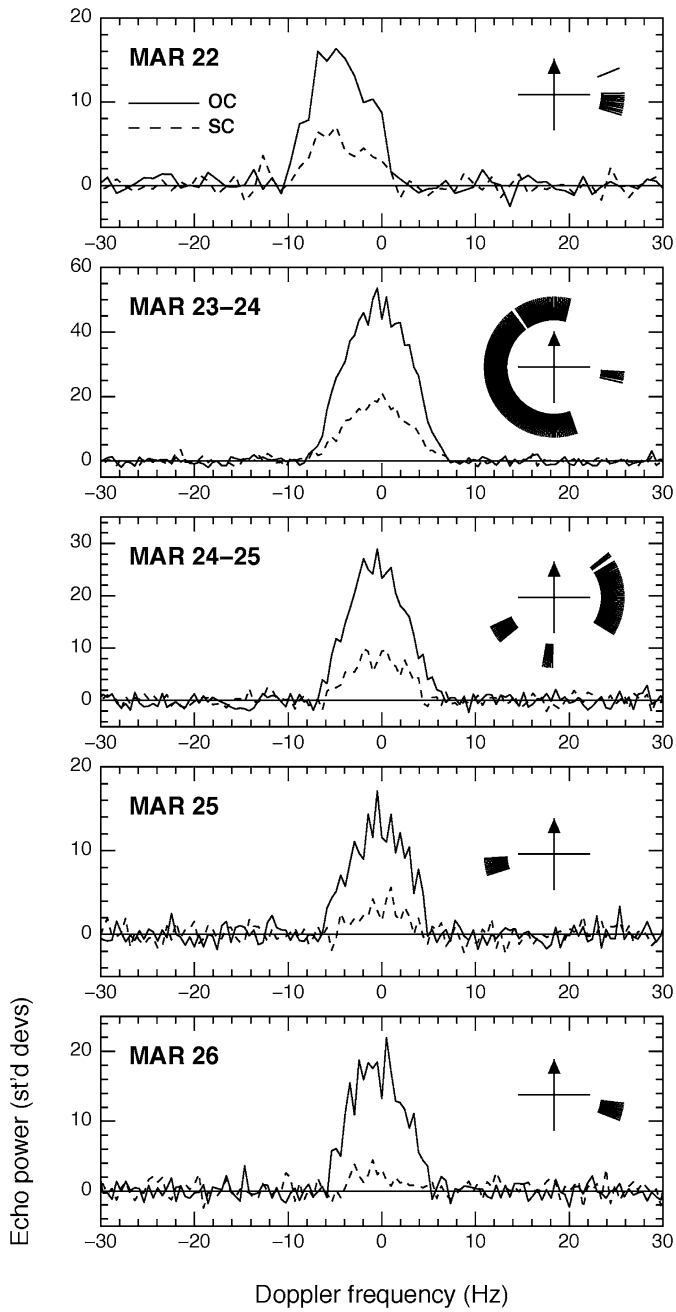

Fig. 1. OC (solid lines) and SC (dashed) echoes, summed over each CW track and normalized to the standard deviation of the noise. The inset charts show rotation phase coverage for each track, referenced to the $+x$ axis of our model. Each radial line represents one transmit–receive cycle. Resolution was 0.98 Hz on March 22 and 0.49 Hz on subsequent tracks.

synthetic radar and lightcurve data that are compared to the observations. The models contain various parameters in addition to those specifying the shape, such as the rotation period, pole direction, and rotation phase. Parameters describing the radar scattering law must be included, because the scattering law affects the structure of the model's radar echo. Ephemeris predictions of where the echo will be located in delay–Doppler space are not perfect, so a series of ephemeris corrections are also necessary.

Table 3
Radar astrometry

Date (UTC)	Observation	Type	Residual (μs or Hz)	Assigned 1-σ uncertainty
Onsite				
1999 3 26 19:00:00	55.88374915 s	Delay	−0.635	3.0 μs
1999 3 26 03:00:00	55.79458404 s	Delay	−0.401	3.0 μs
1999 3 25 20:00:00	55.8392945 s	Delay	−0.593	3.0 μs
1999 3 24 20:40:00	56.5413515 s	Delay	−0.549	3.0 μs
1999 3 24 19:50:00	56.581684 s	Delay	−2.336	6.0 μs
1999 3 24 19:20:00	56.606774 s	Delay	−0.951	10.0 μs
1999 3 23 18:00:00	58.222201 s	Delay	3.200	13.0 μs
1999 3 23 17:20:00	200657.153 Hz	Doppler	0.355	2.0 Hz
1999 3 22 20:20:00	60.196743 s	Delay	−5.003	15.0 μs
1999 3 22 19:00:00	256120.928 Hz	Doppler	−1.058	2.0 Hz
Model				
1999 3 26 23:10:00	−64518.617 Hz	Doppler	0.031	2.50 Hz
1999 3 26 23:10:00	55.96845429 s	Delay	0.107	0.35 μs
1999 3 25 18:30:00	49750.55 Hz	Doppler	−0.023	0.60 Hz
1999 3 25 18:20:00	55.87115177 s	Delay	0.234	0.35 μs
1999 3 24 22:40:00	98798.44 Hz	Doppler	−0.092	0.60 Hz
1999 3 23 19:40:00	189775.86 Hz	Doppler	−0.121	0.60 Hz
1999 3 22 19:10:00	255413.3 Hz	Doppler	−0.359	0.80 Hz

Notes. The upper set of measurements is from visual estimates made during the observations. The lower set of measurements was obtained from shape modeling, and uncertainties derived by measuring the change in chi-square associated with a change in the corresponding parameter. Of these, the final Doppler measurement has a substantially higher uncertainty than the others, because it was produced from delay–Doppler images with lower frequency resolution than the CW data used for the other Doppler values. All measurements correspond to hypothetical echoes received from the asteroid's center of mass and are referenced to the intersection of the azimuth and elevation axes of DSS 14 at Goldstone. One μs in delay corresponds to ∼150 m in range and 1 Hz in Doppler corresponds to ∼18 mm/s at the Goldstone transmitter frequency of 8560 MHz.

Table 4
1992 SK orbital solution (#26)

J2000 heliocentric ecliptic coordinates
Epoch JD 2452676.50000 = 2003 Feb 60.00000

		Post-fit 1-σ	
EC	0.3248962368581255	0.0000000247	
QR	0.8431523524679780	0.0000000326 AU	
TP	2452837.3205205849 JD	0.0000098604 d	(2003 Jul 16.82052)
OM	9.00067416200943	0.0000088471°	
W	233.49726073335935	0.0000122718°	
IN	15.32163831407581	0.0000071645°	
A	1.248922607902554	0.0000000059 AU	
P	509.8022146072290	0.00000362 d	(1.39573793808193 yr)
MA	246.43559060412409	0.0000007023°	

Notes. EC = eccentricity, QR = perihelion distance, TP = time of perihelion, OM = longitude of the ascending node, W = argument of periapsis, IN = inclination, A = semi-major axis, P = orbit period, MA = mean anomaly.

The SHAPE software progressively refines models by adjusting parameters sequentially so as to reduce the sum of the squares of the residuals (chi-square). A model typically goes through several such iterations before an acceptable level of convergence is achieved. Since the modeling process is highly nonlinear, a series of grid searches is required to explore the model parameter space and to map out the locations of various chi-square minima.

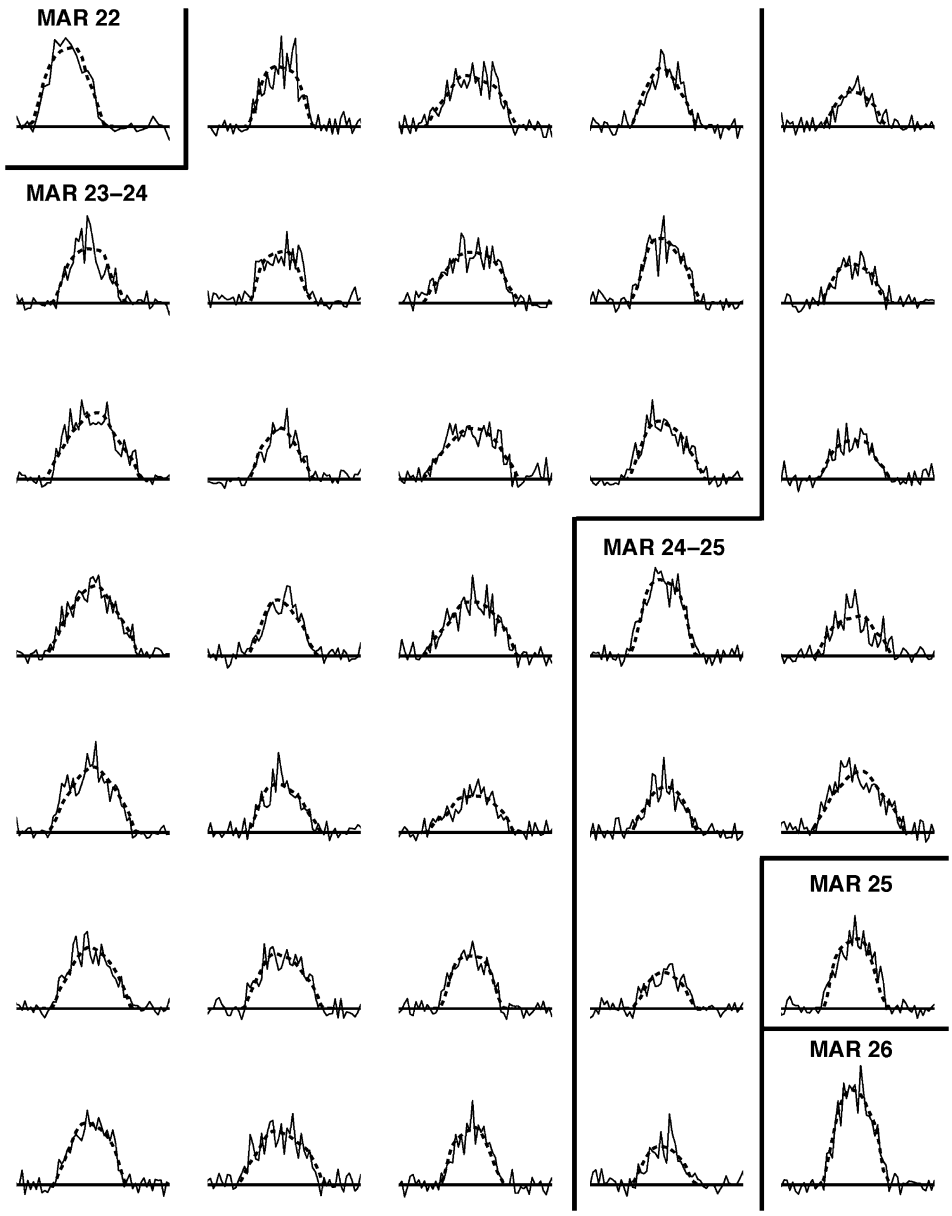

Fig. 2. OC echo power spectra (solid lines) and fits (dashed), separated by observing track. Time increases downward and to the right. All spectra are normalized to the standard deviation of the noise and are at the same scale. The frequency range spans ± 13.5 Hz from the ephemeris position and the vertical axis runs from -3σ to $+23\sigma$. The spectrum from March 22 is at half the resolution of the later spectra and used an older ephemeris with a larger Doppler uncertainty (Table 2).

Lower chi-square can often be obtained with a nonphysical model rather than one that is physically realistic. Penalty functions corresponding to certain physical properties of the model are used by the SHAPE software to control such effects. The penalties are multiplied by weighting factors and added to chi-square to produce an objective function that SHAPE attempts to minimize.

For example, consider the concavity and nonsmooth penalties. SHAPE renders all models as polyhedra. Let θ be the angle between the outward normals of the facets adjacent to an edge. The concavity penalty, defined as the mean over all edges of $\{[1-\cos(\theta)]^2$ if an edge is concave, 0 if an edge is convex$\}$, suppresses facet-scale concavities. The nonsmooth penalty, defined as the mean over all edges of $[1-\cos(\theta)]^4$, suppresses adjacent facets' departure from coplanarity and hence all deviations from a smooth surface.

An accurate model will very likely contain concavities and surface structure at a variety of scales. But if changing a parameter to produce a model with nonphysical protrusions and concavities (for example, a sea urchin) decreases the objective function, then SHAPE will do so. The concavity and nonsmooth penalties constrain such features by increasing the objective function when concavities and protrusions are present. The larger the penalty weight, therefore, the more strongly SHAPE will suppress the corresponding structure. However, if the penalty weights are set too high, the software will produce a model that suppresses real structure. A series of runs at different values of the concavity and other penalties are required. When raising the concavity penalty just starts to decrease the

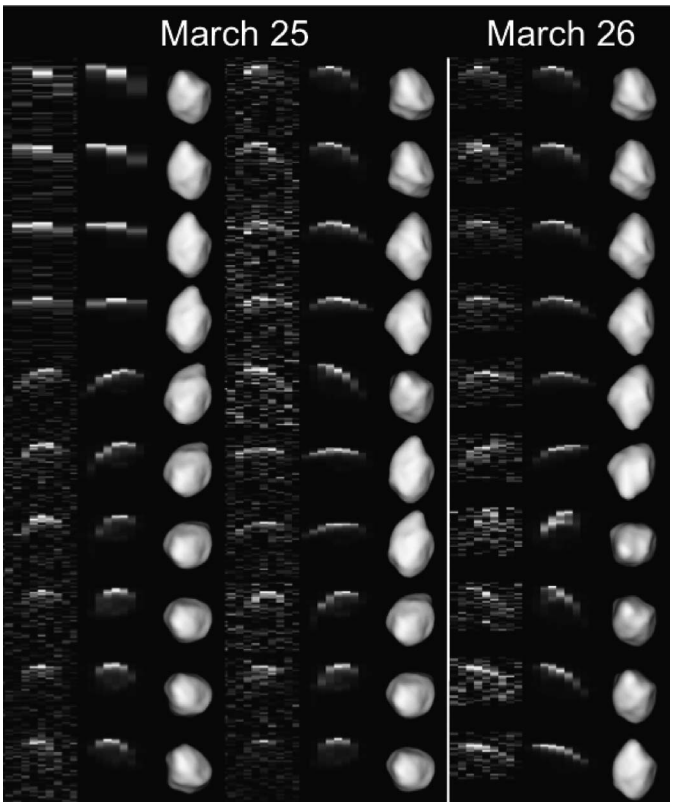

Fig. 3. Goldstone delay–Doppler images, corresponding radar images simulated from the model, and plane-of-sky projections of the model. Delay increases downward and Doppler increases to the right. The pixels are 0.25 μs by 5 Hz for the first 4 images on March 25 and 0.25 μs by 2 Hz for all later frames. The model projections have a plane-of-sky width of 1.5 km and are oriented with north upward and east to the left.

validity of the fits (as determined by chi-square and visual inspection), we can be confident that our model is conservative, but not overly so. That is, we opt to avoid producing structure that is not real (i.e., 'fitting noise') at the price of possibly suppressing real structure.

A crucial factor in the reconstruction inversion is the subradar latitude of the observations. Since the radar images resolve the object only in line-of-sight distance and line-of-sight velocity, if the asteroid were viewed directly on the equator, we would be unable to distinguish between northern and southern sources of a feature in an image. If the asteroid's surface were particularly rugged, there might even be three or more possible source locations. For a series of observations off the equator, however, the delay–Doppler trajectories of features at different positions will differ as the target rotates, and, in principle, their contributions to the image can then be separated. Given enough observations at a variety of rotational phases and at latitudes sufficiently far from the equator, the shape of the visible portion of the asteroid can be reconstructed with confidence. In practice, subradar latitudes several tens of degrees away from the equator are desirable. For the 1999 observations of 1992 SK, our pole direction estimate implies that observations took place between $-20°$ and $-40°$. Therefore, the shape of the asteroid south of about 60° north latitude is well constrained.

Even if the observations take place far enough from the equator that the delay–Doppler trajectories of each point on the asteroid's surface are unique, there may still be regions of the object that cannot be reconstructed with confidence. Portions of the surface that were never seen obviously cannot be modeled and, moreover, even for the visible portion of the object, some regions are less well constrained than others. For portions of the surface that the radar views only at very large incidence an-

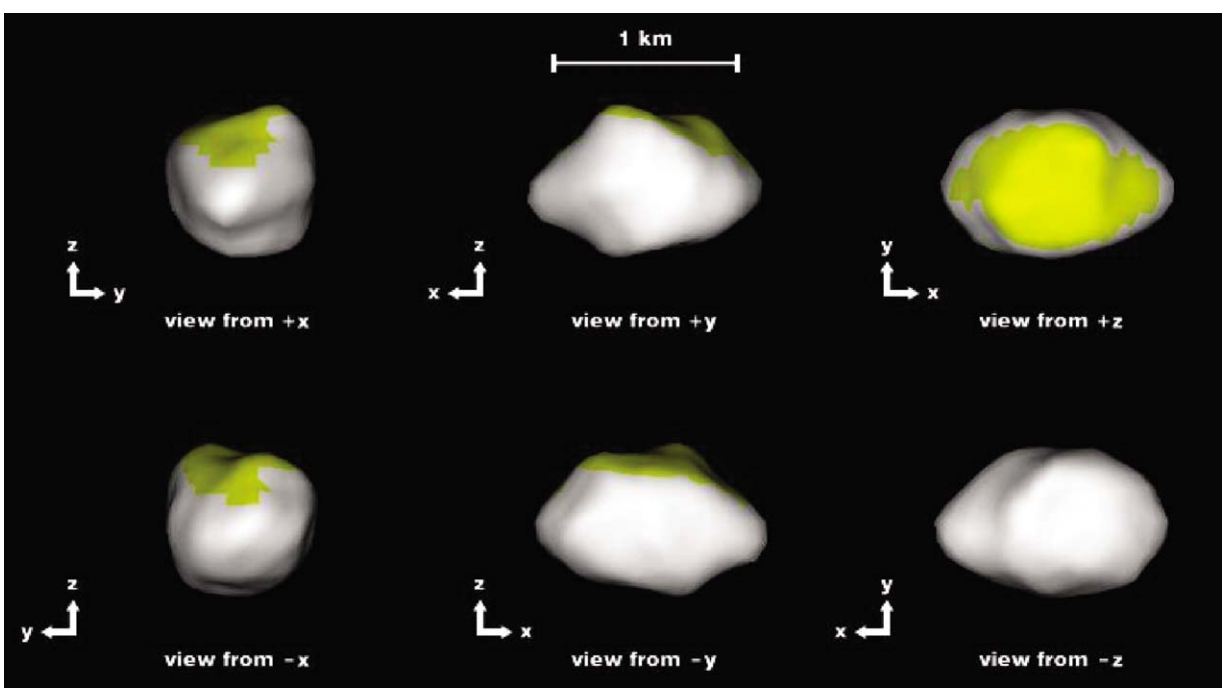

Fig. 4. Principal axis projections of our model. The yellow-shaded regions were seen at incidence and scattering angles greater than 60° or were not seen. This model contains 510 vertices. The renderings have been smoothed and use a Lambertian scattering law.

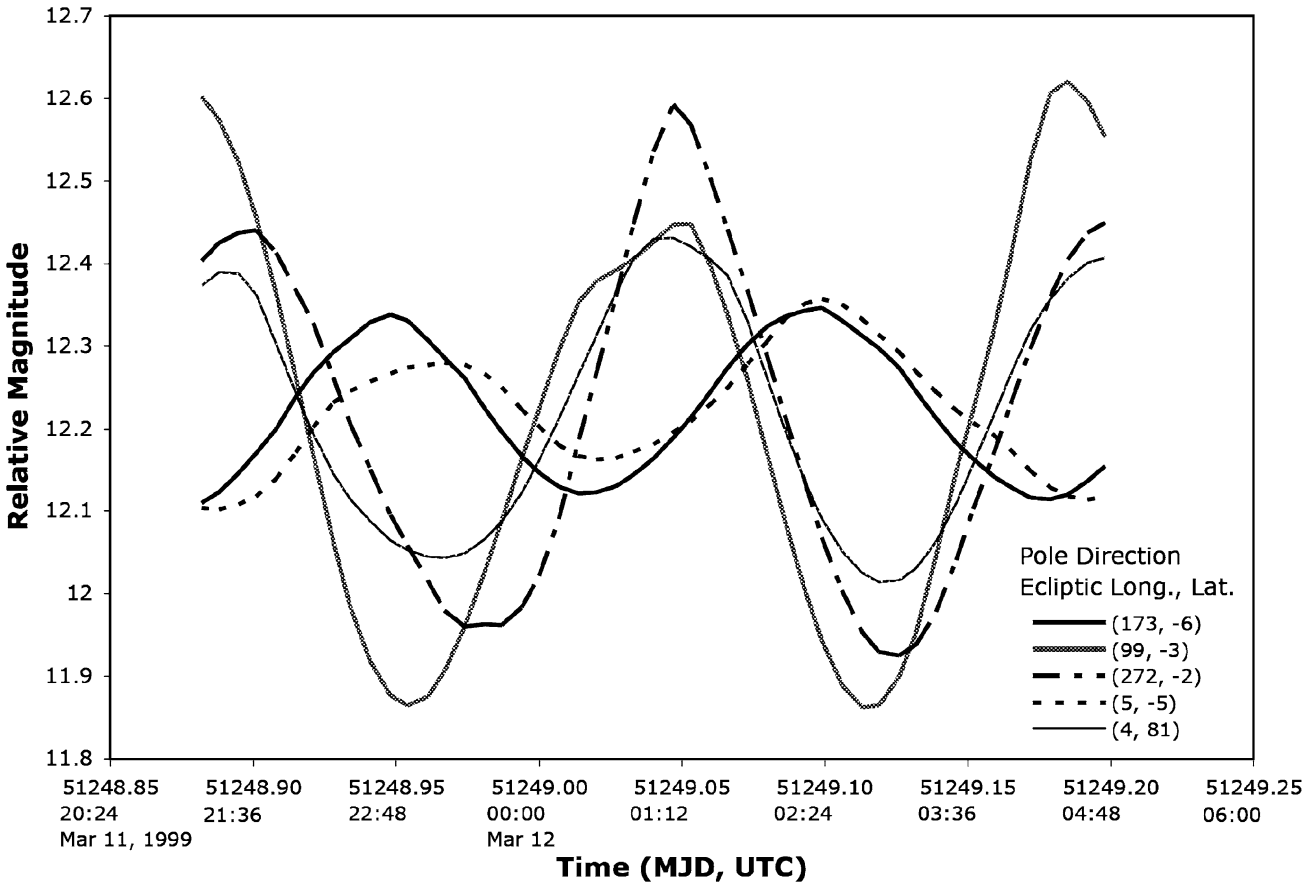

Fig. 5. Model-derived lightcurves for five candidate pole directions from radar-only fitting, over a time span corresponding to one of the observed lightcurves (March 12). Three of the simulated lightcurves have amplitudes significantly smaller than the observed amplitude of 0.8 mag, which rules out those three pole directions.

gles, the echo will be intrinsically weaker. In the principal-axis projections of our model in Fig. 4, the regions shaded in yellow are those that are relatively poorly constrained, either seen at scattering angles greater than 60° or never seen at all. For the lightcurve data, the incidence angle of the sunlight is also important, so only regions where both the incidence and scattering angles were greater than 60° were shaded.

We used a radar scattering law of the form $\rho \cdot \cos^n(\theta)$, where θ is the angle of incidence, an appropriate form because there was no obvious specular reflection in the images. Both the reflectivity ρ and the scattering law exponent n were treated as free parameters. Uncertainties were assigned using changes in chi-square, as with the astrometry. ρ was determined from the CW data only, since the calibration of the images was not as accurate. Each image was adjusted with an arbitrary multiplicative constant so as to minimize chi-square. ρ and n can be used to define an 'equivalent spherical' albedo of 1992 SK; that is, the albedo of a sphere with an identical radar scattering law (Hudson and Ostro, 1994). For our model of 1992 SK, the equivalent spherical albedo is 0.11 ± 0.02.

We modeled 1992 SK as a 510-vertex polyhedron with triangular facets, and adjusted each vertex independently. Some previous asteroid models have used spherical harmonic representations (Hudson and Ostro, 1994), but these cannot model small features as well as a vertex model. Adjusting a spherical harmonic causes a global change in the model's shape, while changing the position of a vertex only affects adjacent facets.

When lightcurves are included in a fit, the model must also include estimates of the visible-wavelength scattering properties of the surface. Although scattering is a very complex process, relatively simple scattering laws can provide reasonable approximations. Our estimation used the scattering law of Kaasalainen et al. (2001), a hybrid between Lommel–Seeliger

Table 5
Properties of the model

OC radar albedo: $0.13 \pm 25\%$
Equivalent spherical radar albedo σ: 0.11 ± 0.02
Smooth-component near-surface bulk density: $\leqslant 2.3\ \mathrm{g\,cm^{-3}}$
Spin state
Pole direction: $(99° \pm 5°, -3° \pm 5°)$
Sidereal period: (7.3182 ± 0.0003) h
Volume: $0.53\ \mathrm{km}^3 \pm 40\%$
Model surface area: $3.4\ \mathrm{km}^2 \pm 30\%$
Diameter of equal-volume sphere: $1.0\ \mathrm{km} \pm 20\%$
Maximum dimensions:
x-axis: $1.39\ \mathrm{km} \pm 20\%$
y-axis: $0.90\ \mathrm{km} \pm 20\%$
z-axis: $0.91\ \mathrm{km} \pm 20\%$

Notes. The equivalent spherical albedo $\sigma = 2\rho/(n+1)$ was calculated using our estimates of the radar scattering law coefficients (Hudson and Ostro, 1994). Both radar albedo values are reasonable for silicate S-class asteroids.

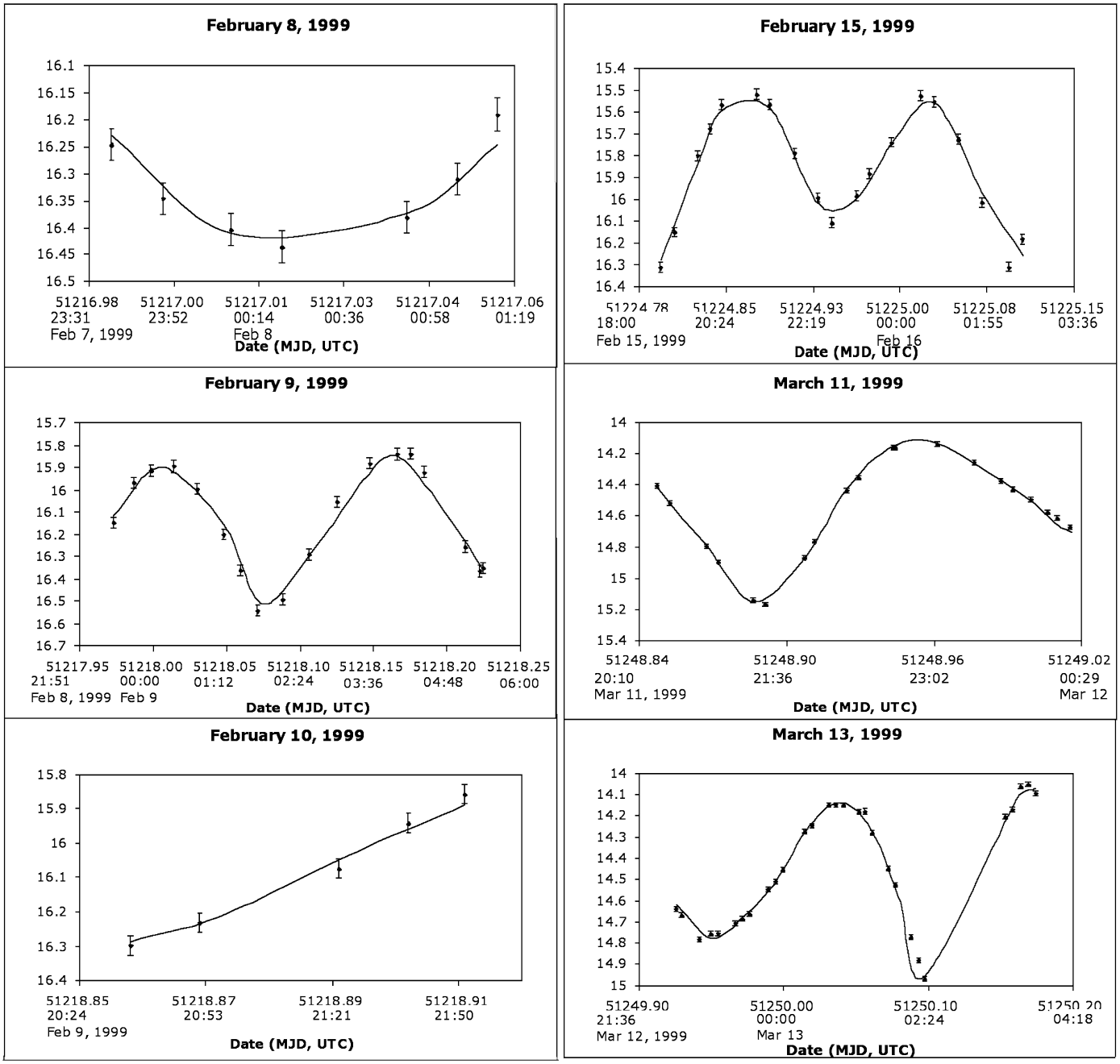

Fig. 6. Optical lightcurves used in the fit. Every 4th lightcurve point is shown. We decimated the lightcurves to allow more rapid fitting. The solid lines are the synthetic lightcurves from our model. Each synthesized lightcurve has been adjusted in magnitude by an additive constant so as to give the best fit to the data.

and Lambertian scattering. This empirical law has proven useful in lightcurve inversion (Kaasalainen and Torppa, 2001; Kaasalainen et al., 2001).

We assumed homogeneous scattering, with no dependence on surface location. Results from other asteroids indicate that a homogeneous scattering law is a good assumption for data similar to ours (Hudson and Ostro, 1994).

We treated the lightcurves as relative photometry. That is, we did not assume a value for the optical albedo, but instead allowed each synthesized lightcurve to "slide" upward or downward in magnitude so as to provide the best possible fit to the data.

4. Modeling results

To reconstruct the shape of an asteroid, we must know the object's spin state or estimate it simultaneously with the shape. For 1992 SK, no pole constraints have been published. However, all of the lightcurves have amplitudes from ∼0.6 to ∼1 mag. Despite the asteroid's sky motion of ∼80°, none of these observations was made close to the pole of the object. Of course, these results exclude only two small portions of the sky. Our analysis used a combination of an all-sky grid search and allowing the SHAPE software to iteratively fit the pole direction. Using the radar data only, we found five widely separated

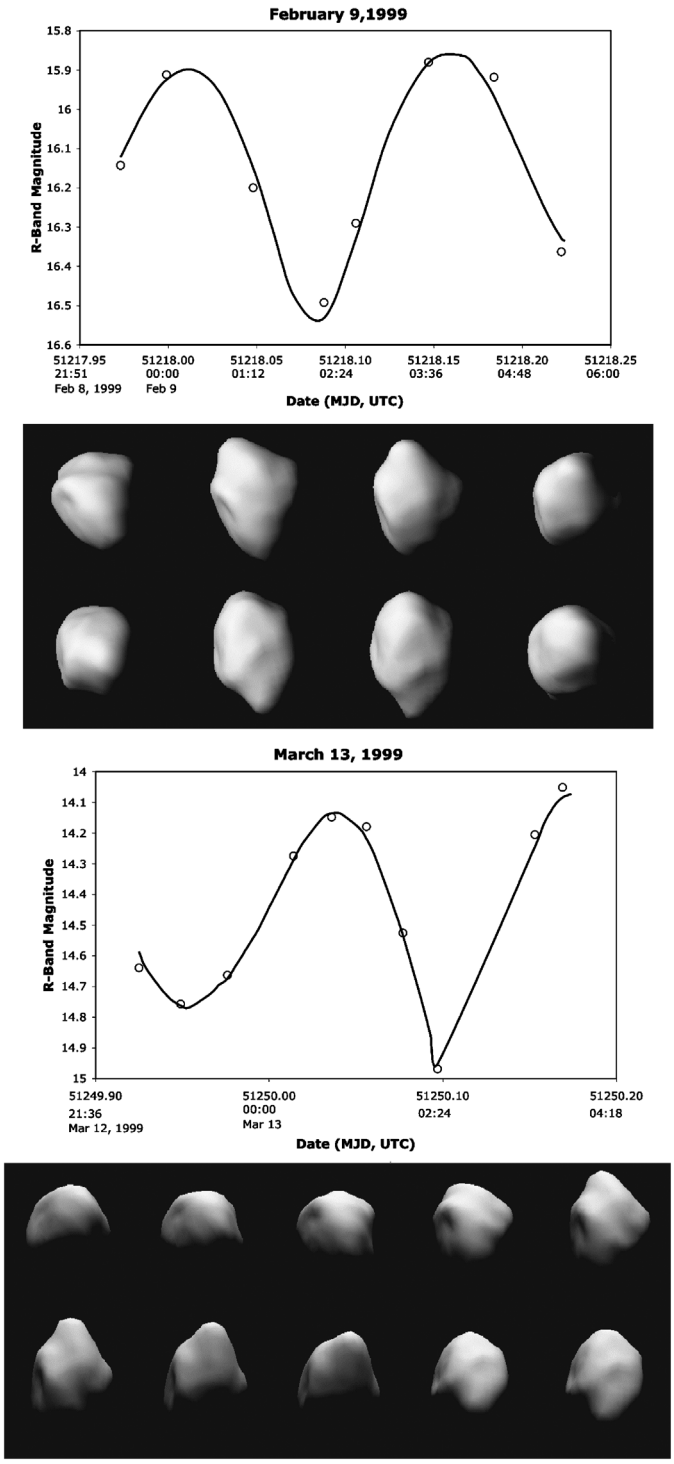

Fig. 7. Plane-of-sky views of the model at the epochs of selected lightcurve observations (open circles). North is up, east is to the left, and time increases from left to right and from top to bottom. The views incorporate the Sun's position (solar phase angle = 42° February 9, 71° March 13) and the Kaasalainen scattering law used in the modeling.

pole directions that produced comparably good fits. However, when we used the corresponding models to produce simulated lightcurves, three of the five pole directions do not produce the required lightcurve amplitude (see Fig. 5) and therefore can be rejected. The remaining two solutions are separated by ∼180° on the sky. Including the lightcurves in the fitting 'splits' the ambiguity between these two solutions and locates the pole direction to within 5° of ecliptic longitude, latitude = (99° − 3°). The lightcurves are also sensitive to the asteroid's rotation period. Treating the period as a free parameter produces dramatic changes in the goodness of fit of the model and allows us to derive a sidereal period of 7.3182 ± 0.0003 h (3σ).

Table 6
Stationary orbits

Equilibrium point	x (km)	y (km)	z (km)	Stability
E1	1.169	−0.073	−0.011	Unstable
E2	0.032	1.112	0.003	Stable
E3	−1.166	−0.053	−0.006	Unstable
E4	0.037	−1.110	0.004	Unstable

Note. Positions (in the asteroid frame) and stability of stationary orbits around our model of 1992 SK, assuming a uniform density of 2.3 g cm^{-3}.

Table 7
March 2006 approach

Date	Subradar latitude (±5°)	RA	DEC	Range (AU)	SNR estimates			
					Goldstone		Arecibo	
					Date	Run	Date	Run
2006 Mar 11	57°	260°	14°	0.121	40	3	860	150
2006 Mar 12	60°	263°	12°	0.118	46	4	910	170
2006 Mar 13	64°	266°	9°	0.115	51	4	930	190
2006 Mar 14	67°	269°	7°	0.113	54	4	810	180
2006 Mar 15	70°	272°	4°	0.111	58	4	560	150

Notes. Subradar latitude is at 00:00 UTC. SNR estimates include our values for the projected area, pole direction and radar albedo. "Run" indicates the maximum SNR per transmit/receive cycle, while "Date" gives the SNR for the weighted mean of all runs on that observing date.

Table 5 lists some properties of our model. Figs. 6 and 7 show the final lightcurve fits and corresponding plane-of-sky views of the model for two of the lightcurves. Fig. 3 shows the model radar images and Fig. 4 shows principal-axis projections of the model. The model is modestly elongated; the protrusion on the $+x$ end of the model is the main contributor to asymmetry in the radar data. The smaller surface features have more significant effects on the lightcurves than on the radar images. Our model's north polar region is poorly constrained, so the structure in that region may be an artifact of the fitting process.

Following Magri et al. (2001), we used the OC radar albedo to set an upper bound of 2.3 g cm^{-3} on the bulk density of the smooth component of the surface. A smooth surface produces only OC echo through single scattering. Multiple scattering and small-scale roughness, which produce all of the SC echo, also produce an unknown portion of the OC echo. However, the density of the rough component of the surface may be higher (rocks) or lower (large pore spaces) than the smooth component, so the total near-surface bulk density and the density of the entire asteroid may be higher or lower than 2.3 g cm^{-3}. [Meteorite analogs for S-class asteroids include stony-irons (specific gravity ∼4.9 g cm^{-3}) and ordinary chondrites (specific gravity ∼3.5 g cm^{-3}) (Ostro et al., 1991).]

Using methods described in Scheeres et al. (1996), we studied the dynamical properties of our model. Our analysis assumed a uniform density of 2.3 g cm^{-3}. A gravitational slope

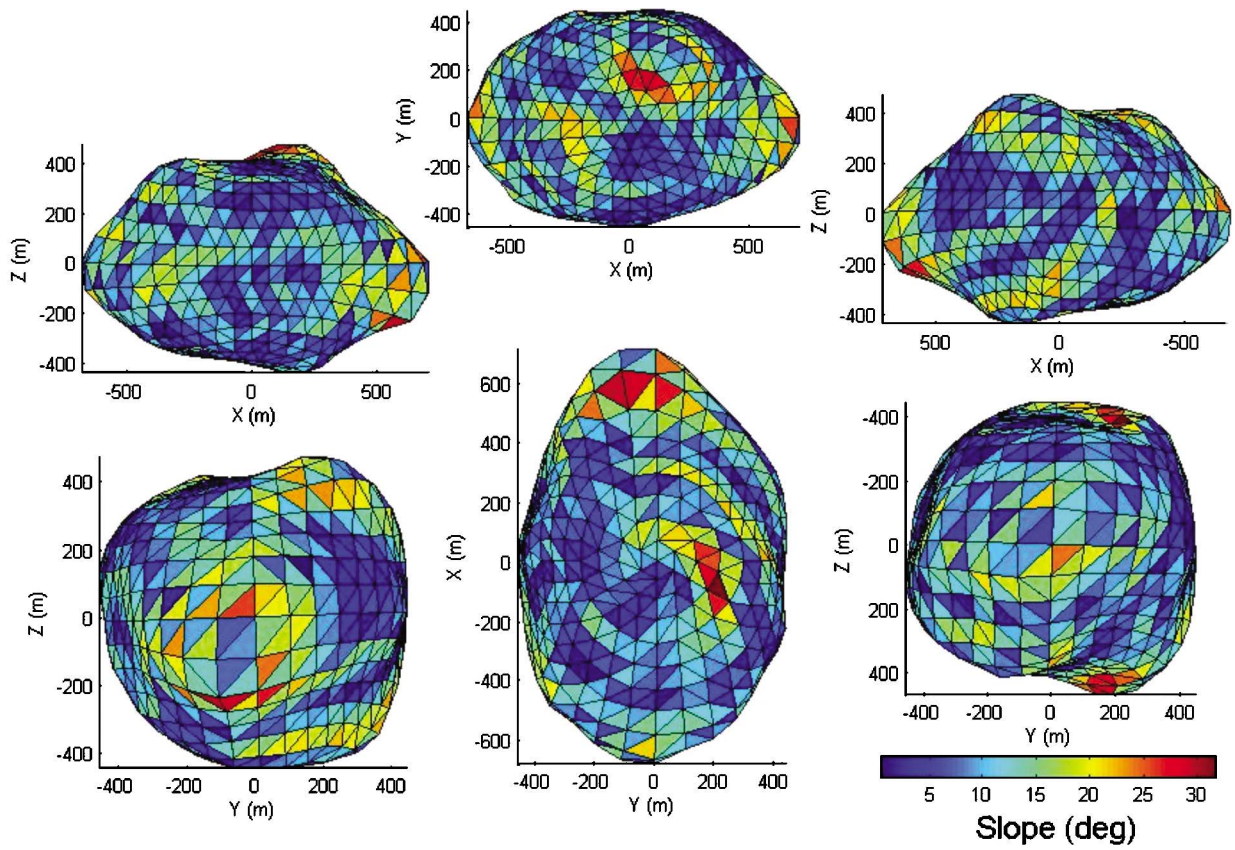

Fig. 8. Gravitational slope mapped over the surface of asteroid 1992 SK, shown in principal axis projections.

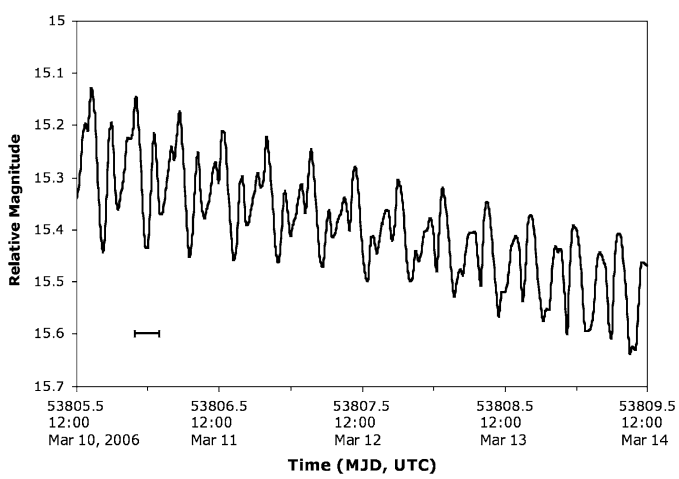

Fig. 9. Predicted optical lightcurves for the 2006 approach. The apparent magnitude of the object decreases gradually due to an increasing solar phase angle. The horizontal error bar represents our 3σ uncertainty in the object's rotational phase.

map of our model is shown in Fig. 8. The slope is defined as the acute angle between the local acceleration vector and the surface normal. The surface of 1992 SK is very subdued, with a maximum slope of 31° and an average slope of 11°. The maximum slope is less than the angle of repose for granular material, so our model does not constrain the subsurface structure of the asteroid. Surface acceleration varies over (2.30 to 3.26) $\times 10^{-4}$ m s^{-2}. Some of the variation is caused by rotational acceleration. The escape speed of the asteroid varies from 0.26 to 0.37 m s^{-1} across the surface.

We also explored our model's close-orbit dynamics. For almost all uniformly-rotating asteroids, there are four close stationary orbits in the frame of the asteroid, which generally lie close to the axes of minimum and intermediate moment of inertia (along the x- and y-axes in Fig. 8). For the majority of asteroids, either two or all four of these equilibria points are unstable. However, our model of 1992 SK has three unstable equilibria points (see Table 6) and therefore occupies an intermediate state.

Our results for the stationary orbits are somewhat dependent on the bulk density of the object. If the bulk density is as low as 1.9 g cm^{-3}, then all of the equilibria are closer to the surface and are unstable. If the bulk density is higher, around 3 g cm^{-3}, then two of the equilibria are stable and all are further from the asteroid.

The close orbit dynamics and gravitational slopes are sensitive to the concavity at the north pole. If the concavity, which has a volume only a few percent of the volume of the asteroid, is largely an artifact, then the positions of the equilibria change slightly and the model is closer to a state with two stable stationary orbits. Filling in the concavity also removes one of the regions of highest gravitational slope. The slopes in other regions of the surface, such as near the south pole, are relatively unaffected. The 2006 observations should provide information on the extent of the concavity and consequently refine our modeling of 1992 SK's gravitational slopes and close-orbit dynamics.

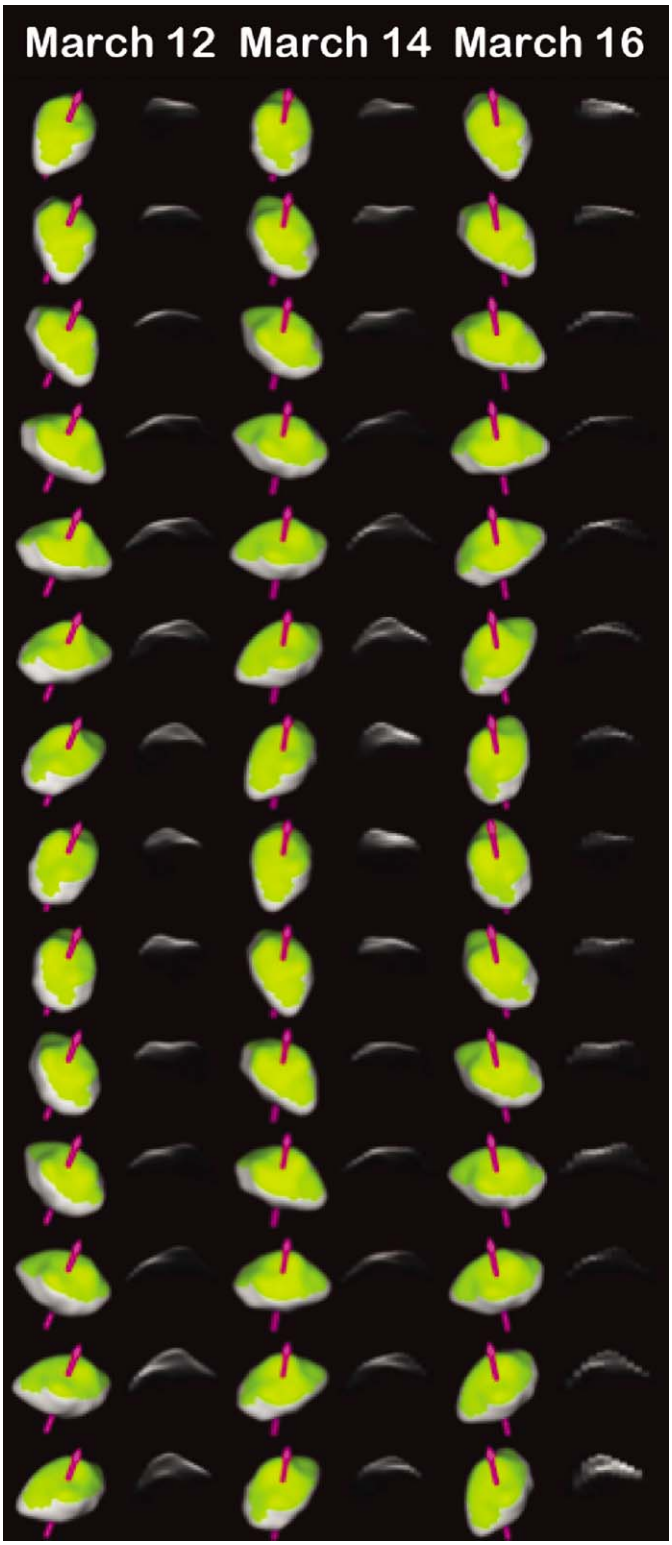

Fig. 10. Predicted Arecibo radar images and plane-of-sky views of the model during the 2006 approach. Each column shows nearly one full rotation, from the beginning of March 12, 14, and 16 UTC (left to right). Images are spaced every 30 min and assume our nominal period. Resolution is 0.1 μs by 0.1 Hz and the rotational phase is uncertain by 100°. Images are oriented as in Fig. 3. The double-ridged feature is caused by the concavity at the north pole. The yellow-shaded regions were seen during the 1999 apparition at incidence and scattering angles greater than 60° or were not seen. Our nominal spin axis is shown on each POS view.

5. Predictions for the 2006 approach

Our inferences about 1992 SK can be evaluated during the asteroid's March 2006 apparition. Although not as close as the one in 1999, the 2006 approach will nevertheless produce signal-to-noise ratios (SNRs) of several hundred per day using the Arecibo 2380-MHz system.

During this approach, the northern half of the object, and the poorly constrained regions of the present model, will be facing Earth (Table 7). Figs. 9 and 10 show predictions of the lightcurves and delay–Doppler images that can be obtained.

Our lightcurve predictions are more accurate in February and early March than they are during the closest approach. During February, the viewing angles are closer to the equator and the poorly constrained north pole has less effect on the measurements. The uncertainty in the period is such that asteroid's rotational phase can be predicted only to within 100° (3σ). The lightcurve amplitude is well determined, but the higher-frequency variations in brightness are due to the poorly constrained structure near the north pole.

The best days for radar observation are March 11–15, after which the asteroid moves out of Arecibo's declination window. The SNR does not drop very much prior to this because the subradar latitude continues to increase, decreasing the echo bandwidth and increasing the SNR as one over the square root of the bandwidth. We estimate that delay–Doppler imaging at resolutions of 0.1 μs (15 m in range) and 0.1 Hz should be readily obtainable. Like the model, some portions of the predicted images are better constrained than others. Since the subradar latitude is so high, poorly constrained regions are closest in range and the leading edge of the echo is uncertain. In addition to providing a test of the modeling from the 1999 data, 2006 data naturally can be combined with the 1999 data to refine this paper's results.

Acknowledgments

We thank the technical staff at Goldstone for help with the radar observations. This material is based in part upon work supported by the National Aeronautics and Space Administration (NASA) under the Science Mission Directorate Research and Analysis Programs. C. Magri was partially supported by NSF grant AST-0205975. The work at Ondřejov has been supported by the Grant Agency of the Czech Republic, Grant 205/05/0604, and by the Grant Agency of the Czech Academy of Sciences, Grant A3003204. Part of this research was conducted at the Jet Propulsion Laboratory, California Institute of Technology, under contract with NASA. M.W. Busch was partially supported by the University of Minnesota Space Grant Consortium.

References

Binzel, R.P., Rivkin, A.S., Stuart, J.S., Harris, A.W., Bus, S.J., Burbine, T.H., 2004. Observed spectral properties of near-Earth objects. Icarus 170, 259–294.

Helin, E., 1992. 1992 SK. IAU Circ. 5628.

Hudson, S., 1993. Three-dimensional reconstruction of asteroids from radar observations. Remote Sens. Rev. 8, 195–203.

Hudson, R.S., Ostro, S.J., 1994. Shape of Asteroid 4769 Castalia (1989 PB) from inversion of radar images. Science 263, 940–943.

Kaasalainen, M., Torppa, J., 2001. Optimization methods for asteroid lightcurve inversion. I. Shape determination. Icarus 153, 24–36.

Kaasalainen, M., Torppa, J., Muinonen, K., 2001. Optimization methods for asteroid lightcurve inversion. II. The complete inverse problem. Icarus 153, 37–51.

Magri, C., Consolmagno, G.J., Ostro, S.J., Benner, L.A.M., Beeney, B.R., 2001. Radar constraints on asteroid regolith compositions using 433 Eros as ground truth. Meteorit. Planet. Sci. 36, 1697–1709.

Ostro, S.J., Campbell, D.B., Chandler, J.F., Hine, A.A., Hudson, R.S., Rosema, K.D., Shapiro, I.I., 1991. Asteroid 1986 DA: Radar evidence for a metallic composition. Science 252, 1399–1404.

Ostro, S.J., Hudson, R.S., Benner, L.A.M., Giorgini, J.D., Magri, C., Margot, J.-L., Nolan, M.C., 2002. Asteroid radar astronomy. In: Bottke, W.F., Cellino, A., Paolicchi, P., Binzel, R.P. (Eds.), Asteroids III. Univ. of Arizona Press, Tucson, pp. 151–168.

Pravec, P., Wolf, M., Sarounova, L., 1998. Lightcurves of 26 near-Earth asteroids. Icarus 136, 124–153.

Scheeres, D.J., Ostro, S.J., Hudson, R.S., Werner, R.A., 1996. Orbits close to Asteroid 4769 Castalia. Icarus 121, 67–87.